ELSEVIER

Contents lists available at ScienceDirect

Acta Materialia

journal homepage: www.elsevier.com/locate/actamat



Full length article

Alloying effects on the transport properties of refractory high-entropy alloys

Prashant Singh ^{a,b,*}, Cafer Acemi ^b, Aditya Kuchibhotla ^b, Brent Vela ^b, Prince Sharma ^{a,c}, Weiwei Zhang ^d, Paul Mason ^d, Ganesh Balasubramanian ^c, Ibrahim Karaman ^b, Raymundo Arroyave ^b, M. Cynthia Hipwell ^e, Duane D. Johnson ^{a,f}

- ^a Ames National Laboratory, U.S. Department of Energy, Iowa State University, Ames, IA 50011, USA
- ^b Department of Materials Science and Engineering, Texas A&M University, College Station, TX 77843, USA
- ^c Department of Mechanical Engineering and Mechanics, Lehigh University, Bethlehem, PA 18015, USA
- ^d Thermo-Calc Software Inc., 4160 Washington Rd, Suit 230, McMurray, PA 15317, USA
- ^e J. Mike Walker'66 Department of Mechanical Engineering, College Station, TX 77843, USA
- f Department of Materials Science & Engineering, Iowa State University, Ames, IA 50011, USA

ARTICLE INFO

Keywords: High-entropy alloys Transport properties Density-functional theory CALPHAD Time-domain Thermoreflectance

ABSTRACT

Additive Manufacturing (AM) has opened new frontiers for the design of refractory high-entropy alloys (HEAs) for high-temperature applications. The thermal conductivity of the AM feedstock is among the most important thermo-physical properties that control the melting and solidification process. Despite its significance, there remains a notable gap in both computational and experimental research concerning the thermal conductivity of HEAs. Here, we use density functional theory (DFT) to systematically investigate the alloying effects on the transport properties of Ti-Cr-Mo-W-V-Nb-Ta RHEAs, including electrical and thermal conductivities and Seebeck coefficient. The relaxation time of charge carriers is a key underlying parameter determining thermal conductivity that is exceedingly challenging to predict from first principles alone, and we thus follow the approach by Mukherjee, Satsangi, and Singh [Chem Mater 32, 6507 (2022)] to optimize the relaxation time for RHEAs. We validated thermal conductivity predictions on elemental solids, binary and ternary alloys, and RHEAs and compared them against thermodynamic (CALPHAD) predictions and our experiments with good correlations. To understand observed trends in thermal conductivity, we assessed the phase stability, electronic structure, phonon, and intrinsic- and tensile strength of down-selected RHEAs. Our electronic structure and phonon results connect well with the observed compositional trends for thermal transport in RHEAs. Our DFT assessment and CALPHAD predictions provide a unique design guide for RHEAs with tailored thermal conductivity, a critical consideration for AM and thermal-management applications.

1. Introduction

Multi-principal element alloys, also known as high-entropy alloys (HEAs), introduced by Yeh et al. [1] and Cantor et al. [2], are typically defined to have principal elements ≥ 3 with concentrations ranging between 5 and 35 at.%. This class of alloys has emerged as a promising candidate for applications in extreme environments [3]. Their complex chemistries result in simple yet highly distorted (at the atomic scale) crystal structures, i.e., face-centered cubic (FCC) or body-centered cubic (BCC), that lead to extraordinary material properties, having high fracture toughness [4] and showing good combinations of strength and

ductility [5,6]. The chemical complexity and atomic size mismatch also result in local lattice distortions that may inhibit diffusive mass transport, helping HEAs retain their structural properties at very high temperatures [7,8], radiation dose rates [9], or corrosive environments [10].

Research on refractory HEAs (RHEAs) has recently gained momentum, as several alloys within this vast chemical space have been shown to exhibit high strength, high oxidation resistance, wear resistance, and/or thermal stability at elevated temperatures [11–25]. Such attributes make RHEAs exceptionally suitable for advanced applications that require high-temperature load-bearing capabilities, such as in

https://doi.org/10.1016/j.actamat.2024.120032

Received 25 January 2024; Received in revised form 20 May 2024; Accepted 22 May 2024 Available online 23 May 2024

1359-6454/© 2024 Acta Materialia Inc. Published by Elsevier Ltd. All rights are reserved, including those for text and data mining, AI training, and similar technologies.

^{*} Corresponding author at: Ames National Laboratory, U.S. Department of Energy, Iowa State University, Ames, IA 50011, USA. *E-mail addresses*: psingh84@ameslab.gov, prashant40179@gmail.com (P. Singh).

aviation, energy applications, and engine manufacturing, as well as for plasma-facing structural materials in nuclear environments. However, RHEA-based parts are difficult to manufacture with standard ingot metallurgy due to their brittleness and high ductile-to-brittle transition temperatures (DBTT) as well as their extraordinary strengths at high temperatures. As such, AM offers an alternative for fabricating defect-free RHEA parts, although several challenges remain [26–29]. Due to their inherent brittleness, for example, RHEAs have a tendency to form cracks upon fast cooling during AM. The thermal shock resistance of RHEAs can be improved through the tuning of their thermo-mechanical properties, including thermal conductivity.

Experimental studies on the thermal transport properties of Refractory High Entropy Alloys (RHEAs) are limited [30–34], even though understanding the impact of chemical complexity on these properties is essential for their high-temperature performance. Thermal conductivity in RHEAs, influenced by charge chemistry and electron and phonon interactions [35], is key for managing thermal stresses and heat dissipation [36–39]. The wide range of thermal conductivities in RHEAs highlights the need for developing predictive design methodologies and their experimental validation, aimed at optimizing RHEAs for specific applications [40–42].

In this study, we conducted a comprehensive high-throughput (HTP) analysis using density-functional theory (DFT) to investigate the effects of alloying on the phase stability and transport properties of Refractory High Entropy Alloys (RHEAs). Specifically, this work is just one study within a larger closed-loop campaign in which we designed RHEAs for application in jet engine turbine blades [43]. This assessment is crucial for the design of RHEAs with optimized thermal management and enhanced additive manufacturability, particularly for high-temperature applications [44,45]. The HTP DFT calculations were complemented with CALPHAD-based predictions. The investigation was carried out refractory-containing 126 alloys within over Cr-Hf-Mo-Nb-Ta-Ti-V-W-Zr system. The transport properties of interest include electrical conductivity, thermal conductivity, and Seebeck coefficient, which depend inherently on the relaxation time of the energy/charge carriers. We evaluated the temperature-dependent relaxation time by analyzing the electronic thermal conductivities of elements in periodic-table groups five (V, Nb, Ta) and six (Cr, Mo, W).

We complemented the thermal conductivity analysis with easy-to-calculate quantities from DFT and mean-field methods, i.e., phase stability, intrinsic (elastic moduli), and yield strength, to capture their correlation. Such correlations are important as they can be exploited for alloy design [46–48]. Focusing on RHEAs with melting temperatures above 1800° C, we investigated their electronic structure and phonons to understand alloying effects on thermal conductivity. We offer a theoretical analysis of the transport properties in RHEAs with experimental validation. We provide insights for designing novel high-temperature structural alloys that advance our understanding of optimizing high-performance alloys in thermal environments.

2. Methods

2.1. Density functional theory (DFT)

We employed first-principles DFT as implemented in the Vienna Abinitio Simulation Package (VASP) [49,50] for geometrical optimization (e.g., lattice constants, volume, bond length, and bond angles) and charge self-consistency. The generalized gradient approximation of Perdew, Burke, and Ernzerhof (PBE) was employed in all calculations [51] with a plane-wave cut-off energy of 520 eV. The choice of PBE over LDA or meta-GGA [52,53] functionals is based on the work of Söderling et al. [54] and Giese et al. [55] that establishes the effectiveness of GGA functionals. Large Supercell Random Approximates (SCRAPs) ranging from 54 to 90 atoms per cell to accommodate non-stoichiometric compositions with optimized disorder (zero-correlation) [56] were generated (a single, optimized configurational representation) for DFT

calculations. We used energy and force convergence criterion of 10^{-6} eV and 10^{-6} eV/Å, respectively, for full (volume and atomic) relaxation of MPEA SCRAPs. The Monkhorst-Pack k-mesh was used for Brillouin zone integration during structural optimization and charge self-consistency calculations [57].

DFT-based perturbation theory (DFPT) calculations were combined with PHONOPY code to analyze phonon dispersion and phonon density of states of three selected MPEAs, i.e., CrMoNb, Nb $_{50}$ Mo $_{25}$ V $_{20}$ W $_{5}$ [58]. The disorder supercells of these three alloys were further optimized with stricter energy and force criterion of 10^{-8} eV and 10^{-7} eV/Å as phonon calculations needs zero lattice and atomic forces.

2.2. DFT enthalpy calculations

Formation energy (E_{form}) of selected compositions were calculated:

$$E_{form} = E_{Total}^{HEAs} - \sum_{i} n_{i} E_{i}$$
 (1)

here E_{Total}^{HEAs} is the total energy of disordered BCC RHEAs, n is the number of atoms in the SCRAPs configuration, and E_i is the elemental energy. E_{form} per atom was calculated by dividing by the number of atoms per unit cell.

2.3. Transport properties

Electronic thermal conductivity (κ_e) and electrical conductivity (σ_e) of electrons were calculated using the BoltzTraP code [59] for the Boltzmann transport equation, obtained by integrating the following equations:

$$\sigma(T;\mu) = -\frac{1}{V} \int_{-\infty}^{\infty} d\varepsilon \times \sigma(\varepsilon) \frac{\partial f(T,\varepsilon,\mu)}{\partial \varepsilon}$$
 (2)

$$\kappa(T; \mu) = -\frac{1}{e^2 TV} \int_{-\infty}^{\infty} d\varepsilon \times \sigma(\varepsilon) \times (\varepsilon - \mu)^2 \frac{\partial f(T, \varepsilon, \mu)}{\partial \varepsilon}$$
 (3)

Here, V is the volume per unit-cell, μ is alloy chemical potential, T is temperature, and ε is the electronic band energy. The conductivity tensor $\sigma(T;\mu)$ is defined in terms of the projected density of states energy, i.e., $\sigma(T;\mu) = \frac{1}{N_e} \sum_k \sigma(k) \delta(\varepsilon - \varepsilon_k)$, where N_e is DFT carrier concentration calculated, and the k points in the k-mesh.

2.4. Lattice thermal conductivity

We computed the lattice thermal conductivity (LTC) of RHEAs using the Slack model [60,61].

$$\kappa_l(\theta_a) = \frac{4.04311}{20\pi^3(1 - 0.514\gamma^{-1} + 0.228\gamma^{-2})} \times \left(\frac{k_B\theta_a}{\hbar}\right)^2 \frac{k_B M_{av} V^{1/3}}{\hbar \gamma^2}$$
(4)

Here, LTC is dependent on Grüneisen constant (γ) [62], acoustic Debye temperature (θ_a) [63], average atomic mass (M_{av}) , and volume per atom (V) at a given temperature. The acoustic Debye temperature can be estimated from the Debye model using Bulk moduli (B) as [64–66]

$$\theta_a = n^{1/3}\theta_D = n^{1/3} \frac{h}{k_B} [6\pi^2 V^{1/2} n]^{1/3} f(\nu) \sqrt{\frac{B}{M_{av}}}$$
 (5)

Here, n is the number of atoms in the unit cell, ν is the Poisson's ratio, and $f(\nu)$ is the compressibility factor given by

$$f(v) = \left\{ 3 \left[2 \left(\frac{2}{3} \times \frac{1+\nu}{1-2\nu} \right)^{2/3} + \left(\frac{1}{3} \times \frac{1+\nu}{1-\nu} \right)^{3/2} \right]^{-1} \right\}^{1/3}$$
 (6)

 ν is estimated using the rule-of-mixture from elements, typically in

the range 0.25-0.35. The bulk modulus of each RHEA was obtained directly from DFT calculations.

2.5. Alloys studied

In this work the transport properties of 126 refractory-containing alloys were studied with DFT. These alloys are reported in the Supplemental Materials. These alloys were synthesized throughout the course of a close-loop campaign aimed at designing RHEAs for application in jet engine turbine blades. These alloys were down-selected for various purposes throughout the closed-loop campaign. Of these 126 alloys, 106 were designed throughout the RHEA discovery campaign itself and are, at a minimum, predicted to meet the constraints shown in Table 1. While the closed-loop campaign itself is not the subject of this work, thermal conductivity is an important consideration in this campaign and must be well understood prior to committing resources to scale-up any candidate alloys for further investigation.

The remaining 21 alloys were selected for various reasons to supplement the design campaign. Among these alloys, 5 are non-equimolar ternaries systematically selected to refine Thermo-Calc's TCHEA4 thermodynamic database. Specifically, after applying variations on the filters outlined in Table 1, we targeted ternary systems that most frequently appeared within the passing design space. These systems, which were previously not critically assessed in TCHEA4, were identified as important to the success of the campaign. These alloys are denoted by the tag 'CALPHAD' in the Supplemental Material. Thus, ternary systems with the 'CALPHAD' tag are frequently represented in the alloys with the 'Designed' tags. These thermodynamic assessments were subsequently incorporated into the TCHEA5 and TCHEA6 databases. Assessment of these ternaries is important to ensure that the quaternary and quinary alloys meet the BCC phase stability constraint in Table 1. The remaining 14 alloys were selected according to expert opinion and metallurgical intuition based on the performance of the designed alloys. These alloys are denoted with the tag 'Other'. All compositions and their predicted properties are reported in the Supplemental Material. Details on this closed-loop campaign will be published in future work, however for the scope of this work, the transport properties of this chemically diverse set of 126 refractory-containing alloys were systematically studied with DFT.

2.6. CALculation of PHAse diagrams (CALPHAD)

The CALPHAD method involves calibrating free-energy models. These linear models are derived from theories and phase-dependent parameters, which can come from experimental data or various modeling approaches. These parameters are associated with derivatives of Gibbs free energy and include factors like chemical potential, enthalpy, specific heat capacity, and volume. In the present work Thermo-Calc's freeze-in temperature model equipped with the TCHEA5 database was used to estimate thermal conductivity for 126 candidate RHEAs. These alloys were designed to have a single BCC phase at

Table 1 Constraints applied to down select the designed alloys. κ ; room temperature thermal conductivity. P; room temperature density. $T_{solidus}$; solidus temperature. YS; Yield strength.

Constraint	Purpose	Information Source
$\kappa \geq 12~ ext{W/m-K}$	Thermal management (motivation for work)	Thermo-Calc Property Module
$\rho \leq 11~g/cc$	Application in aircraft	Thermo-Calc Property Module
$T_{solidus} \geq 1800^{\circ} C$	High temperature operation	Thermo-Calc Property Module
Single Phase BCC at 1300°C and T _{solidus}	Avoid deleterious phases	Thermo-Calc Equilibrium Module
$YS \ge 150 \text{ Mpa at } 1300^{\circ}\text{C}$	High temperature operation	Maresca-Curtin Model

1300°C, as predicted by Thermo-Calc's equilibrium model (for more details on this design process, see Ref. [67]). As such, the freeze-in temperature was set to 1300°C to calculate the thermal conductivity of the BCC phase at various temperatures and compositions. To capture temperature dependence of thermal conductivity, the Thermo-Calc property model queries polynomials that are functions of temperature that are fitted on thermal conductivity data for unaries and end-member compounds in the CALPHAD database. When relying on this database of experimental thermal conductivities, electronic and lattice thermal conductivities are not treated separately. When data is sparse for a particular system, the thermal conductivity is estimated to a first approximation by the Slack model [61,68,69] for lattice thermal conductivity and the Wiedemann-Franz Law [61,68] for electronic thermal conductivity, which is then summed to obtain the overall thermal conductivity [68].

2.7. Experimental details

Five RHEA compositions selected for experiments were synthesized from high-purity elements (>99.9 wt.%) using a Buehler AM200 vacuum arc melter (VAM) under ultra-high purity (UHP) Argon (Ar) atmosphere. Each coupon was flipped and remelted at least 10 times to ensure compositional homogeneity. Vanadium (V), the lightest element in the candidate alloys, was added to the melt last to minimize evaporation losses during fabrication. Homogenization heat treatments were performed in an UHP Ar atmosphere using a Centorr high-temperature furnace (LF Series, Model 22). The heat treatment chamber was vacuumed and flushed with UHP Ar gas 3 times before each cycle. The heat treatment time and temperature selections were guided by the diffusion module of Thermo-Calc software, DICTRA, to fully eliminate the dendritic structure, imaged using a scanning electron microscope and analyzed for dendrite dimensions. Following the heat treatments, the alloys were furnace-cooled down to room temperature. Density measurements of the bulk arc-melted coupons were carried out using the Archimedes method with an analytical balance equipped with a density determination kit after heat treatments. Ethanol ($\rho = 0.789 \text{ g/cm}^3$) is used as the immersion liquid. Subsequently, sample profiles were cut via wire electrical discharge machining (wire-EDM) to produce 10 mm by 10 mm specimens with 2mm thickness for microstructural and compositional investigation and thermal property measurements. The specimen surfaces were polished using abrasive SiC polishing papers starting from 320 grit to produce a final polish with 1200 grit. Samples were then placed into a vibratory polisher for 48 hours in 0.04 µm colloidal silica suspension. The sample surfaces were cleaned using an ultrasonic cleaner for 15 minutes in an isopropanol bath at 50°C before the measurements were performed.

The specific heat capacity of the samples was measured using a TA Instruments DSC 2500 scanning calorimeter, covering a temperature range from 15 to 40°C at a ramping rate of 20°C/min. Room-temperature thermal conductivity was measured using Time-domain Thermoreflectance (TDTR). Before conducting TDTR measurements, the polished side of the sample was coated with a \sim 90-nanometer-thick layer of Al, which served as the TDTR transducer. TDTR, an advanced laser-based pump-probe technique, can determine the thermal properties of bulk and nanostructured materials [70,71].

As shown in Fig. 1, this technique involves periodically heating the sample surface with a modulated pump laser beam while a delayed probe laser beam detects the resulting temperature changes on the surface through the thermoreflectance of a transducer. The determination of thermal transport properties is accomplished by adjusting free parameters (the unknown thermal properties) in a thermal transport model [72] to obtain the best fit between the model prediction and the experimental data. This process extracts thermal properties such as thermal conductivity and interface thermal resistance. Thermal conductivity measurements were conducted three times at various locations on the sample to confirm repeatability. The acquired signal is then

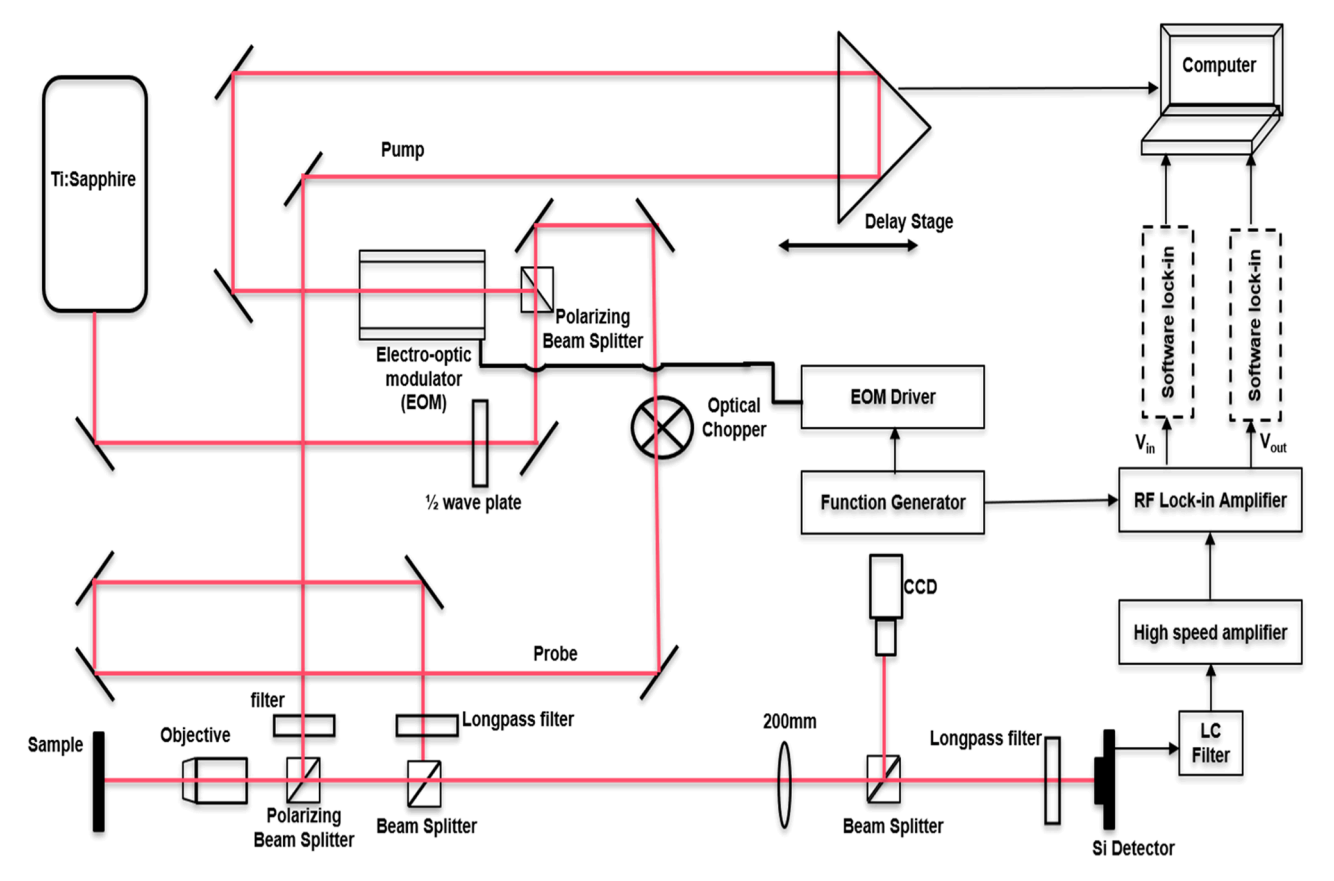


Fig. 1. Schematic of the Time-Domain Thermoreflectance (TDTR) testing apparatus at Texas A&M University. A mode-locked Ti:Sapphire laser is divided into pump and probe beams to heat and measure thermo-reflectance change successively. Optical filters block the pump beam from reaching the Si photodiode.

processed using an analytical heat-transfer solution of the sample structure to deduce important parameters, like thermal conductivity (κ) and the thermal boundary conductance (TBC) at the metal transducer-sample interface. When measuring the cross-plane κ of the sample, we utilized a $10\times$ objective with a spot size of $10.3~\mu m$, and the pump beam is modulated at a frequency of 9.6 MHz. To determine the thicknesses of the Al transducer, we employed a picosecond acoustic technique profilometry [71]. The microstructure of the samples was investigated using FEI Quanta 600 FE-SEM with a voltage of 20kV. An Oxford Instruments energy dispersive X-ray spectroscopy (EDS) system equipped with X-ray mapping and digital imaging was used to determine the average compositions of synthesized alloys after heat treatments.

3. Results and discussion

3.1. Section I – thermal transport properties of refractory based multiprincipal element alloys

In theoretical estimations of (electronic) thermal conductivities, the relaxation time (τ_e) is often treated as a constant; however, it should be treated as a function of temperature and electronic states due to its dependence on scattering events and its related electronic origin. Accounting for the temperature dependence of relaxation time is important as both electrical conductivity and thermal (electrical) conductivities are directly proportional to τ_e . In practice, conductivity data from experiments is fitted to a "back-calculated" τ_e . Clearly, this approach is not useful in high-throughput studies due to insufficient conductivity data for chemically complex alloys. To address this lack of data, we took the machine-learning (ML) model proposed by Mukherjee et al. [73] and fit it with DFT-calculated quantities to predict τ_e of RHEAs in a high-throughput manner. The final model resulted in the relation:

$$\tau_e \sim 3.5 \times 10^{-3} \times T^{-1} \times n^{-1/3},$$
 (7)

where T is temperature and n ($\sim n_{e-}/V$) are carrier concentration. The relaxation time of Cr, Mo, and W in Fig. 2a shows a weakly increasing trend with increasing atomic number, indicating its dependence on the change of electron concentration with increasing temperature. The ML model in [39] had the dependence on charge carrier, unit-cell volume, and temperature, where charge carrier and V were calculated from DFT.

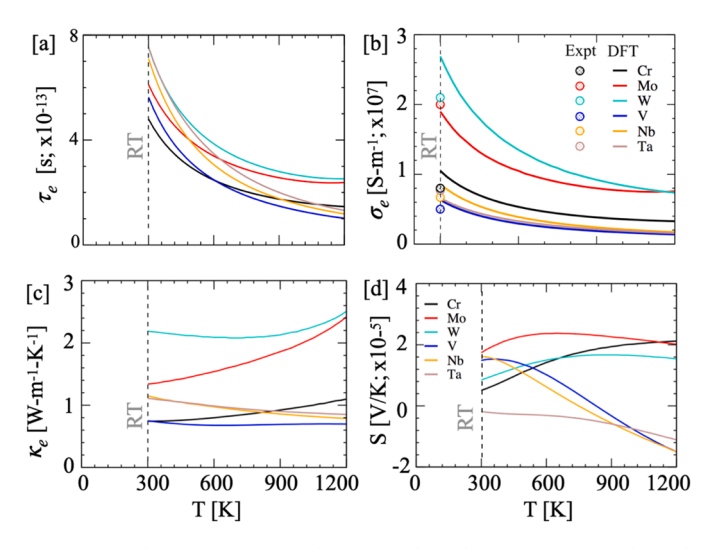


Fig. 2. (a) Relaxation time (τ_e) , (b) electrical conductivity (σ_e) , (c) Thermal (electrical) conductivity, and (d) Seebeck coefficient (S) of group five (V, Nb, and Ta) and group six (Cr, Mo, W) elements of the periodic table. Room-temperature σ are compared with experiments [74].

For simplicity, we excluded contributions due to scattering on grain boundary and point-defects, as we are considering near defect-free single-phase alloys with large grain size. We also want to clarify that the relaxation time in this work includes the effects arising from charge carriers.

In Fig. 2a, the model estimated range of τ_e was found to be of the order of 10^{-13} s for group five (V, Nb, and Ta) and group six (Cr, Mo, W) elements, consistent with the range observed in metallic materials. We found that the relaxation time at higher temperatures (>1000K) is significantly reduced compared to RT data in Fig. 2a. We found a quick drop in τ_e due to an increase in scattering with increasing temperature up to 600 K. On the other hand, if we exclude Ta, the high-temperature behavior of τ_e for each element remains the same due to insignificant changes in scattering after a certain temperature. The elemental electrical conductivities (σ) calculated from the model plus DFT-predicted relaxation are shown in Fig. 2b. The DFT-predicted σ was compared to room-temperature data from experiments and exhibited good agreement [74].

The DFT-calculated electronic thermal conductivity (κ_e) estimate in Fig. 2c was done using the relaxation time model in Eq. (7), which shows a slight change in trends compared to electronic conductivity in Fig. 2b. The Mo shows lower conductivities (σ_e , κ_e) compared to Cr and W, i.e., Mo $(\sigma_e, \kappa_e) < \text{Cr } (\sigma_e, \kappa_e) < \text{W} (\sigma_e, \kappa_e)$. We traced back this change to varying unit-cell volumes, number of charge carriers, atomic size mismatch, and atomic mass differences among unary Cr, Mo, and W. It was well known that the thermal (electronic) conductivity in any materials can be determined by the transfer of energy through electronic collisions with atoms as well as with electrons themselves. These electronic collisions are expected to become more frequent with increase in temperature, thereby, leading to electronic conductivity dependence on both composition and temperature. Additionally, our analysis of the Seebeck coefficient (S), depicted in Fig. 2d, reveals that negative (positive) Seebeck coefficient values indicate holes (electrons) as the predominant charge carriers. A similar trend is observed in group five elements of the periodic table with body-centered cubic (bcc) crystal symmetry, namely V, Nb, and Ta. Notably, these elements, which have analogous electronic configurations, also exhibit a similar range of relaxation times.

As pointed out earlier, it is important to understand how chemistry change in refractory based metal alloys impacts transport behavior. In Fig. 3, we show the change in DFT calculated transport behavior including relaxation time (Fig. 3a), electrical conductivity (Fig. 3b),

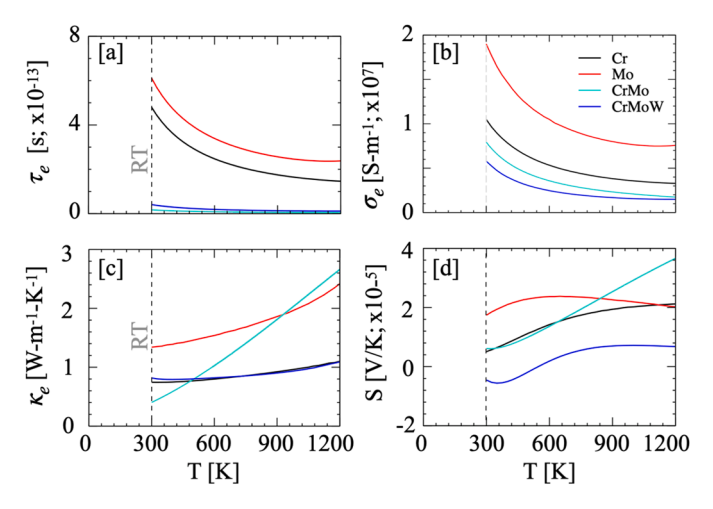


Fig. 3. (a) Relaxation time (τ_e) , (b) electrical conductivity (σ_e) , and (c) thermal (electrical) conductivity (κ_e) with increasing chemical complexity, i.e., Cr, Mo, CrMo, CrMoW. Conductivity changes due to W addition arise from specific mass and charge balancing in CrMoW. Tungsten is at the eighth place overall in terms of electrical conductivity (e.g., $\sigma_{e,W}$ is 31% of Cu).

thermal (electrical) conductivity (Fig. 3c), and Seebeck Coefficient (Fig. 3d) of unary (Cr, Mo), binary (CrMo), and ternary (CrMoW) refractory alloys. The relaxation time of unary was found one order of magnitude larger than binary and ternaries. While electrical conductivity of ternary CrMoW (\sim 0.6 \times 10⁷ S/m) RHEA in Fig. 3b shows a factor of two-to-three drop compared to unary (\sim 1.1-1.9 \times 10⁷ S/m) and a factor of 1.2 drop compared to binary (10⁶ S/m) alloy. Interestingly, a weakly increasing trend in thermal (electrical) conductivity was observed for most cases except for binary CrMo in Fig. 3c, which shows a sharp increase with temperature. These changes could be attributed to varying electron scattering abilities arising from differences in atomic sizes and valence-electrons in unary, binary, and ternary metal alloys.

We also analyzed the Seebeck coefficient (S), which depends directly on type of charge carriers. Our analysis for CrMoW (Fig. 3d) shows that holes are the effective charge carriers controlling the Seebeck behavior at low-T (< 500 K) while electrons are the effective charge carriers high-T (> 500 K). We found that ternary refractory CrMoW shows strong tunability of transport with respect to increasing chemical complexity when compared to unary {Cr, Mo, W} or binary {CrMo, CrW, MoW} alloys (see electronic structure reference in appendix Fig. A1). For example, the weak thermal (electrical) conductivity for the ternary CrMoW in Fig. 3c is attributed to an increased chemical (positional) disorder that aids the creation of new conducting paths. At high energy sites, the new electronic mechanism created by disorder leads to an increased probability of carriers, which is expected to decrease the electrical conductivity due to increased chemical complexity [75]. We believe that the slow change in thermal (electrical) conductivity with temperature originates from disorder such as chemical and/or mass disorder, atomic-size mismatch, varying valence-electron etc introduced by increasing chemical complexity. Thus, in the next section, we tried to understand the origin of these trends in terms of electronic structure, i. e., DFT calculated charge density (carrier density) and density of states.

3.2. Section II - electronic-structure correlation of electrical conductivity

The increased disorder, i.e., chemical and lattice, arising from alloying and different atomic sizes introduces local lattice distortions in the periodicity of the BCC RHEAs, which leads to elastic scattering of the conduction electrons at an extremely fast rate at finite temperature. This provides the primary scattering mechanism for electronic transport phenomena in metallic alloys. To understand the change in transport behavior with a systematic increase in chemical complexity, we plot the total density-of-states (DOS) for Cr, Mo, CrMo, and CrMoW (Fig. 4a), while alloy charge density difference ($\Delta \rho \left[alloy - \sum_i elements_i \right]$) (Fig. 4b) shown for CrMo and CrMoW, which is calculated with respect to elemental constituents.

Fig. 4a shows the energy dependence of the total electronic DOS in disordered CrMo and CrMoW. The elemental DOS for Cr and Mo are shown as a reference to highlight the alloying effects. The increased electronic DOS for CrMo and CrMoW compared to Mo at the Fermi level is the possible reason for reduced electrical conductivity (Fig. 3b) and Seebeck coefficient (Fig. 3d). This hypothesis also connects well as lower DOS for Mo at/near Fermi-level shows higher conductivity. This shows an inverse correlation between total DOS and electrical transport. We believe that increased electronic states in disordered solids enhance the local scattering, reducing the overall conductivity. To understand it better, we plot the charge density difference for CrMo and CrMoW in Fig. 4b, which shows that CrMoW has a much higher electronic density that would lead to higher electronic scattering and lower transport. With increasing temperature, a lower conductivity (higher resistivity) in Fig. 3b found for CrMoW indicates that the increased atomic-level disorder in the ternary alloy results in a higher degree of disorder smearing. This corroborates with our hypothesis that chemical complexity provides better control on tunability of thermal transport in RHEAs.

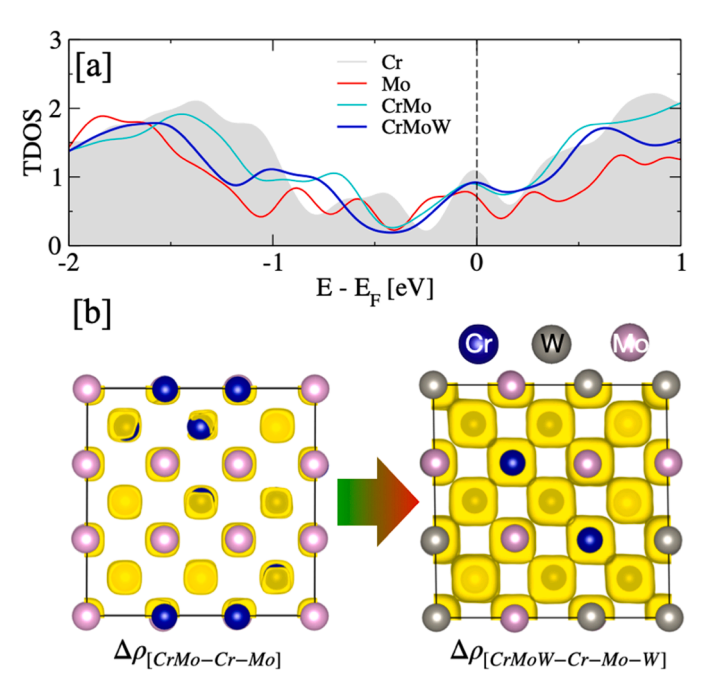


Fig. 4. (a) Electronic density of states, and (b) charge density difference $(\Delta \rho)$ is shown for unary, binary and ternary refractory alloys. For direct comparison, we used isosurface value of 0.12 e-/Å³ to plot $\Delta \rho$ for CrMo and CrMoW (see more details in appendix Fig. A1).

3.3. Section III – comparison of electrical conductivities: DFT and ${\it CALPHAD}$

The electrical conductivity in metal alloys is proportional to the Wiedemann-Franz (W-F) relation, where free electrons are the primary carriers responsible for electrical conduction. The W-F relation establishes the proportionality between thermal and electrical conductivities arising from changes in carrier concentration. Moreover, we know that both electrical and thermal conductivities in metals are due to the flow of charge carriers within a given lattice structures. We plot a comparative electrical conductivity for CrMoX (X=W, Ta, V, Nb) RHEAs calculated using DFT (Fig. 5a) and CALPHAD in (Fig. 5b.). The increased chemical complexity in CrMoX shows significant variation in room temperature electrical conductivity, i.e., $0.4-1.5 \times 10^7 \text{ S-m}^{-1}$. We attribute this change in electrical conductivity to a significant change in valence electron distribution and atomic-size mismatch found in group-V (V, Nb, Ta) and group-VI (Cr, Mo, W) elements of the periodic table. It is well known that the conduction phenomena in a disordered alloy are governed by valence electrons, where the mean energy of electrons depends on the system temperature. For the five alloys in Fig. 5b, we

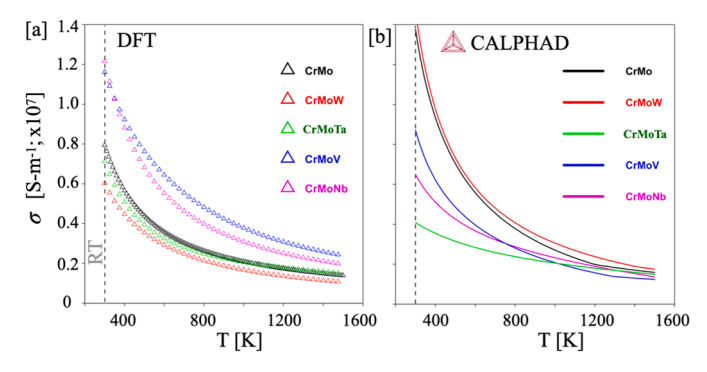


Fig. 5. Comparison of (a) DFT and (b) CALPHAD calculated electrical conductivities of binary and ternary refractory alloys, i.e., CrMo, CrMoW, CrMoTa, CrMoV, and CrMoNb.

found that higher VEC systems (CrMo, CrMoW) show higher conductivity while lower VEC systems (CrMoX, X=V, Nb, Ta) show lower conductivity. Notably, the conductivity clearly finds its connection to the charge carriers, which is suggestive of direct role of valence electrons. The slight difference between DFT and CALPHAD calculated electrical conductivities arises from differences in relaxation time that needs optimized unit-cell volume and charge-carrier information as shown in Eq. (1). Despite such differences, we found similar range of electrical conductivities between our DFT based approach with CALPHAD.

3.4. Section IV - transport analysis of CrMoX and Cr-/Mo-based RHEAs

3.4.1. CrMoX based ternary refractory alloys

Here, we analyze the transport behavior of medium entropy CrMoX (X=Ti, Zr, V, Nb, Ta, W) and Cr-/Mo-based RHEAs. In Fig. 6, we present transport properties, where we systematically investigated the effect of adding group four (Ti, Zr), group five (V, Nb, Ta), and group six (W) elements. In Fig. 6a, we plot the temperature dependence of relaxation time, which shows an order of magnitude jump ($\sim 10^{-12}$ s) compared to unary and binary systems ($\sim 10^{-13}$ s, see Fig.2a and c). Our findings demonstrate the dependence of relaxation time on alloying chemistries, indicating the drawback of the standard assumption of constant relaxation time, especially in RHEAs. However, we do not see a drastic change in relaxation time with a change in the type of alloying elements. The electrical and thermal conductivities for CrMoX are shown in Fig. 6b and c. Both electrical and thermal conductivities of medium entropy CrMoX alloys with group four elements (Ti/Zr with valence electron count of 4) result in much lower values than group five or six alloying additions.

Most (not all) metals are known to have very poor Seebeck coefficients while having significantly higher electrical conductivity. We can see in Fig. 6d that ternary refractory alloys show a very low Seebeck coefficient. Interestingly, Ti/Zr shows negative Seebeck throughout the temperature range (decreases with increasing temperature), which indicates holes as dominant charge carriers, while V/Nb/Ta/W have electrons as dominant carriers. The CrMoW alloy is the only exception, with holes as the dominant carrier at low T and electrons are dominant carriers at high T.

3.4.2. CrMo-based quaternary and quinary RHEAs

In Fig. 7, we plot the transport behavior of six CrMo-based RHEAs, where CrMo composition varies from 35-45 at.% (Cr \sim 5-10 at.% and Mo \sim 25-40 at.%), while all other elements (Ti/V/Nb) are 55-65 at.%.

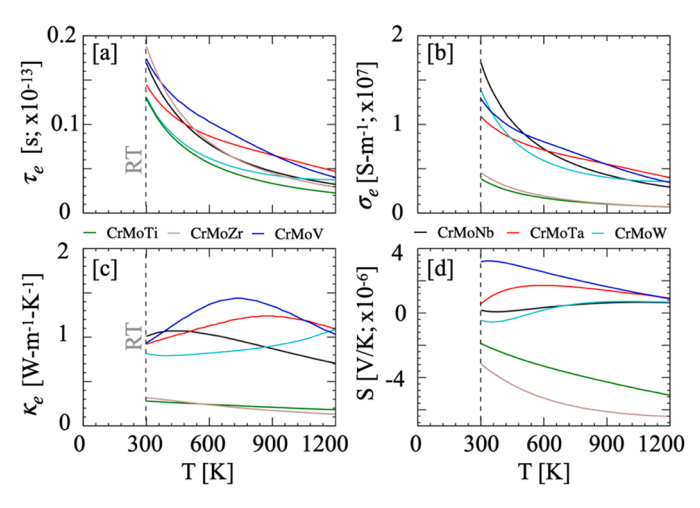


Fig. 6. (a) Relaxation time (τ_e) , (b) electrical conductivity (σ) , (c) thermal (electrical) conductivity (κ_l) , and (d) Seebeck coefficient of medium entropy refractory CrMoX alloys, where X=Ti, Zr, Nb, Ta, W.

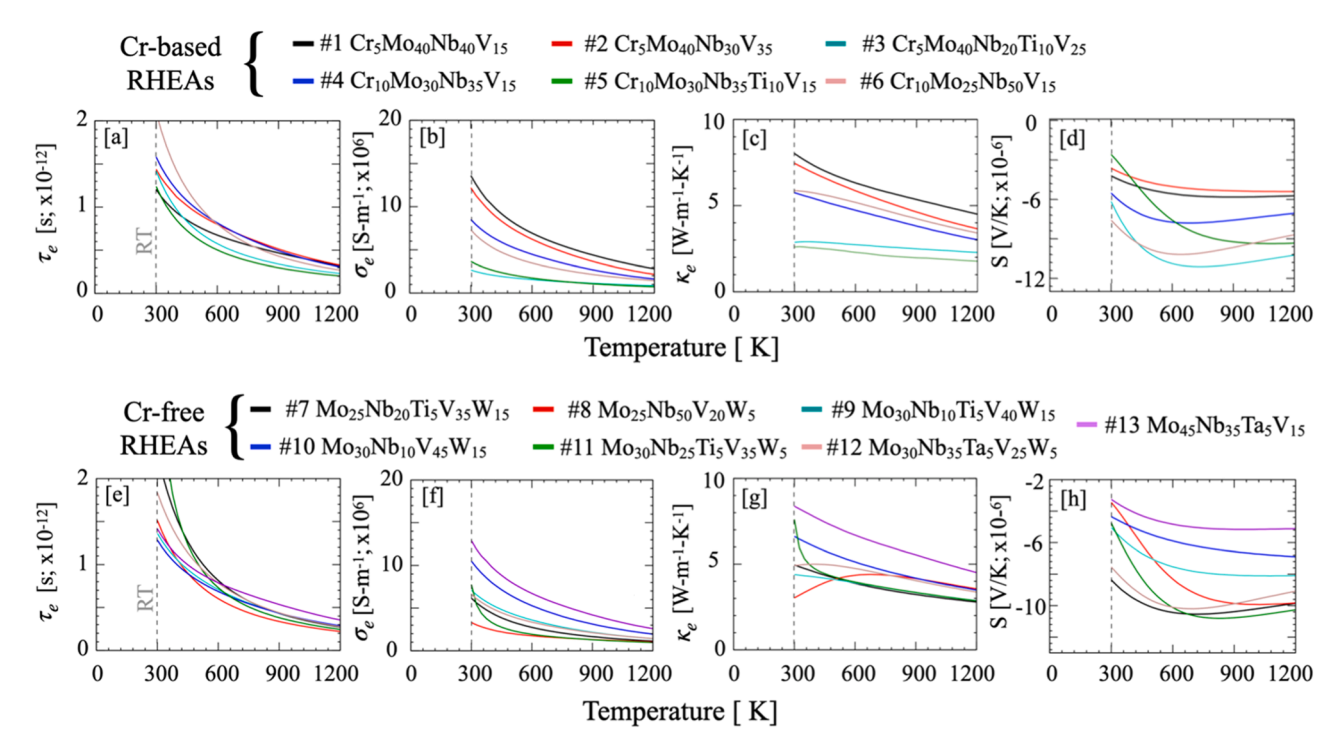


Fig. 7. Relaxation time (τ_e) , electrical conductivity (σ_e) , thermal (electrical) conductivity (κ_e) , and Seebeck coefficient of (a-d) CrMo-rich, and (e-h) MoNb-rich RHEAs.

The selection criteria are based on information provided in Table 1 in the method section. The temperature dependence of relaxation time for CrMo-based RHEAs is shown in Fig. 7a, which shows a similar order of magnitude as ternary alloys in Fig. 6a, i.e., $10^{-12} \rm s$. This indicates that alloying elements do not greatly affect relaxation time after a certain complexity level. We do see slightly higher relaxation time for RHEA6 where at.% CrMo (35) < at.% Nb (50) at low temperatures, probably due to a disproportional increase in the composition of one element. However, the relaxation times of all six RHEAs tend to be in a similar range at high temperatures.

For Cr-based RHEAs, both electrical and thermal conductivities in Fig. 7b & c show monotonic change (decrease) with increasing temperature. We found that alloy #3 ($Cr_5Mo_{40}Nb_{20}Ti_{10}V_{25}$) and #5 ($Cr_3Mo_{30}Nb_{35}Ti_{10}V_{15}$) with 10 at.% Ti shows lower conductivities. This correlates well with our discussion for ternary CoMX (X=Ti/Zr) in Fig. 6b &c, where hole doping (substituting Ti/Zr at X) shows significantly lower conductivities. Similar to the relaxation time in Fig. 7a, both the conductivities seem to converge to similar values at higher temperatures, except for alloys #1 and #2, which are slightly higher than #6.

Interestingly, the Seebeck coefficients show a minimum factor of two reductions compared to the observed range for ternaries in Fig. 6d. We found that the holes are dominant charge carriers in all six RHEAs, which looks obvious from the negative values of Seebeck coefficients. However, the alloy #3 ($Cr_5Mo_{40}Nb_{20}Ti_{10}V_{25}$) and #5 ($Cr_{30}Mo_{30}Nb_{35}$. $Ti_{10}V_{15}$) were found most dominant from the Seebeck coefficient point of view due to considerable variation with increasing temperatures. Our electronic estimate shows that alloy #3 has 0.05 higher electrons, i.e, alloy #5 has more holes reflected in Seebeck plot in Fig. 7d. Higher hole states represent unfilling of electronic states that moves them into the vicinity of Fermi level, making them more temperature sensitive, which is manifested through sharp change in Seebeck coefficient with temperature in Fig. 7d.

3.4.3. MoNb-based (with no Cr) quaternary and quinary RHEAs

The second set of alloys were chosen that has now Cr, and the selection criteria is based on information provided in Table 1 (see the

methods). In Fig. 7e-h, we discuss the transport properties of Mo-based RHEAs with no Cr where Mo composition varies from 25-45 at.%, while all other elements (Ti/V/Nb/Ta/W) are 55-75 at.%. The temperature dependence of relaxation time for Mo-based RHEAs is shown in Fig. 7a. Clearly, the alloys #7, #11, and #12 show slightly higher relaxation times compared to others. Interestingly, all three RHEAs have 5-10 at.% Ti or Ta with W, while other alloys show no such combination. This is a contrasting behavior of Ti in the absence of Cr, as Figs. 6 &7a show no noticeable change in relaxation time in the presence of Cr. We speculate that this behavior is more related to phase stability as Cr (> 10 at.%) leads to energy instability (discussed in the next section). Despite these differences, the order of magnitude remains similar to Cr-based alloys, i. e., $1 \times 10^{-12} - 3 \times 10^{-12}$ s.

The electrical conductivity of Mo-based (no-Cr) RHEAs, in Fig. 7f show monotonic change (decrease) with increasing temperature, which is similar to the observed trends in relaxation time in Fig. 7e. The electrical conductivity trends in Mo-based RHEAs (3 \times 10⁶ - 13 \times 106 S/m) was found to be in a similar range as CrMo-based RHEAs in Fig. 7b (3 \times 10⁶ – 14 \times 10⁶ S/m). The alloys #11 in Fig. 7e-h is the only exception that shows a much sharper drop at lower temperatures, which drops to the level of alloy #8, where the only commonality between #8 and #11 is W composition (5 at.%W). In Fig. 7g, we show the thermal conductivities for seven Mo-based RHEAs. While the alloys #8, #11, and #12 in Fig. 7g show non-monotonic behavior in thermal conductivities. Notably, we found that each RHEA, i.e., alloys #8, #11, and #12, has very low tungsten (5 at.%W), which suggests that these alloys behave very differently at low W concentrations. The Seebeck coefficients for Mo-based alloys in Fig. 7h show further shift on a negative scale compared to Cr-based alloys in Fig. 7d. The major variation in the Seebeck coefficients was found for alloys #7, #11, and #12, which is like the trends observed in relaxation time in Fig. 7e as both the quantities strongly depend on number of charge-carriers.

3.5. Section V – phase stability and thermal conductivity of CALPHAD selected 126 MPEAs

Until this point, we systematically studied the transport properties of a selected set of unary, binary, ternary, quaternary, and quinary alloys to understand the alloying effects on electronic properties. What follows below focuses on the total thermal conductivity (TC; here onward we will use this terminology) of 126 CALPHAD-selected RHEAs using the Slack model [60,61] combined with DFT-calculated electrical and thermal conductivities.

In Fig. 8a, we show a high-throughput formation enthalpy (Eform) analysis of 126 compositions down-selected from CALPHAD-based analysis. The high (positive) formation enthalpy stability in Fig. 8a with increasing Cr composition was detrimental to the thermodynamic stability of Cr-Mo-Nb-Ta-Ti-V-W RHEAs. The E_{form} in Fig. $8\boldsymbol{a}$ can be divided into two distinct regions - (i) enhanced stability of E_{form} with decreasing Cr at.% (x = 0 to 15), and (ii) further substitution of Cr (i.e., beyond 15 at.% Cr) acquires a plateau-like zone (enhanced stability in terms of energetics as compared to the Cr-poor region). Phase stability was also looked at in a bigger context during the analysis by combining it with the compositional variation of other elements with respect to Cr. For example, Mo-, Nb- or V- rich alloys were found to enhance the Cr solubility limit in RHEAs of interest. In Fig. 8b, we show a scatter plot of total thermal conductivity (TC) from CALPHAD and DFT. For hightemperature applications, the minimum required TC is 10-12 W/m-K for efficient heat management in metal alloys [43], which is marked by horizonal and vertical, green-dashed lines. Along with minimum TC criteria, the down-selected RHEAs also satisfy the other requirement required for high-temperature application including phase stability and strength as noted in Table 1.

Fig. 8c shows the comparative plot of CALPHAD and DFT calculated thermal conductivities for 20 selected RHEAs at room temperature. These 20 RHEAs are a subset of the total 126 alloys studied in this work to sample Mo-rich and Cr-rich corners of the alloy design space. The thermal conductivities of these alloys were studied withing DFT, which are marked in the spreadsheet provided in the Supplemental Material. Of these 20 alloys, 5 alloys were selected for experimental validation of thermal conductivity. The selection of alloys for experiments was guided based on strength screening via Vickers microhardness to identify better-performing candidate alloy compositions. The details of other experimental measurements including mechanical properties of the alloys studied in this work will be given in future publication. Notably, a direct correlation was found between thermal conductivity and the amount of Cr, where TC almost increases linearly with Cr and group IV

elements (see appendix Figs. A2 & A3). For some cases, the RHEAs with lower or no Cr (higher Cr) slightly overestimate (underestimate) the TC in DFT when compared to CALPHAD. However, overall, DFT and CALPHAD show a good agreement, which suggests that single-phase approximation in DFT has no visible effect on the overall conclusion. Furthermore, the DFT-predicted TC range combined with the Slack model [60,61] for RHEAs in Fig. 8c was found to be in good agreement with the TC range predicted by Abere et al. [39].

Following transport analysis, we tried to understand the trends in phase stability (E_{form}) and mechanical properties (intrinsic strength and tensile strength) of 20 down-selected RHEAs with respect to varying at. %Cr, as shown in Fig. 9 (see down-selection criteria in method section). Notably, we found two regions in phase stability (E_{form}) in Fig. 9a with Cr-rich (low stability) and Cr-poor (high stability) [76]. Similar trends were observed in intrinsic strength (i.e., bulk moduli; Fig. 9b) [77] and strength (Fig. 9c) [40–42] where alloys with higher Cr concentration possess superior bulk modulus and strength. Interestingly, this shows an inverse correlation between TC (total) (Fig. 8c) and strength (Fig. 9c) in RHEAs (see Appendix Figs. A1 and A2 for detailed comparison of TC with respect Cr composition). Our findings make sense as higher Cr means a freer electron cloud within the alloy, which means higher conductivity.

3.6. Section VI - experimental validation

We conducted TDTR experiments to evaluate the thermal conductivities of 5 chosen RHEA compositions. Alloys were homogenized at 1800°C and 1925°C to eliminate the dendritic microstructure observed in as-cast conditions before conducting the TDTR experiments. The microstructures of the alloys were observed using electron microscopy and found to be dendrite-free and compositionally uniform after the homogenization heat treatments. To analyze the TDTR data, solely two parameters need to be modified for curve fitting: the sample's overall thermal conductivity and the thermal conductance of the Al/allov interface, denoted as G. Within these alloys, G typically falls between 120 and 180 MW/m²K⁻¹, a value aligned with other Al/metal interfaces featuring thin surface oxides. Generally, TDTR determines the thermal effusivity of a bulk sample, which reflects the combined effect of its thermal conductivity and volumetric heat capacity. Density values obtained through Archimedes' principle and room-temperature specific heat capacity measurements were employed to calculate the sample's volumetric heat capacity, serving as input for the TDTR data analysis. The average of three measurements obtained from the specimens and the DFT/CALPHAD predictions for thermal conductivity of the selected

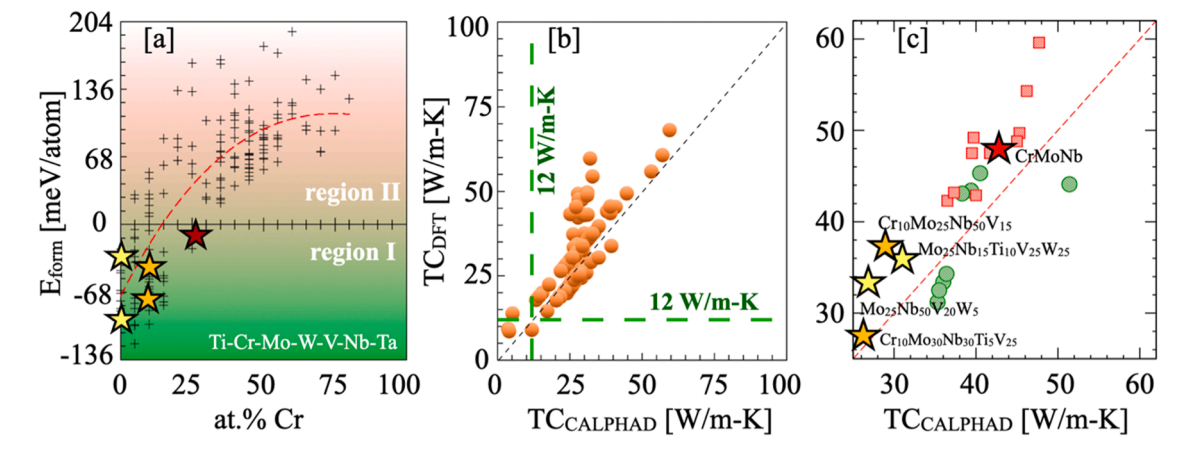


Fig. 8. (a) Formation enthalpy (E_{form} ; meV/atom) of 126 refractory-containing alloys studied in this work with respect to at.%Cr, and (b) a comparative TC plot for 126 RHEAs calculated using CALPHAD and DFT at 300 K. (c) We further select 20 RHEAs from (b) with single-phase stability (-150 meV/atom to +50 meV/atom [5]) and best mechanical properties including yield-strength (>400 MPa [43]), and filter five RHEAs for thermal conductivity testing. The color gradient in (a) shows that phase stability is stable (unstable) in green region I (red region II). 5 down-selected compositions for experimental validation.

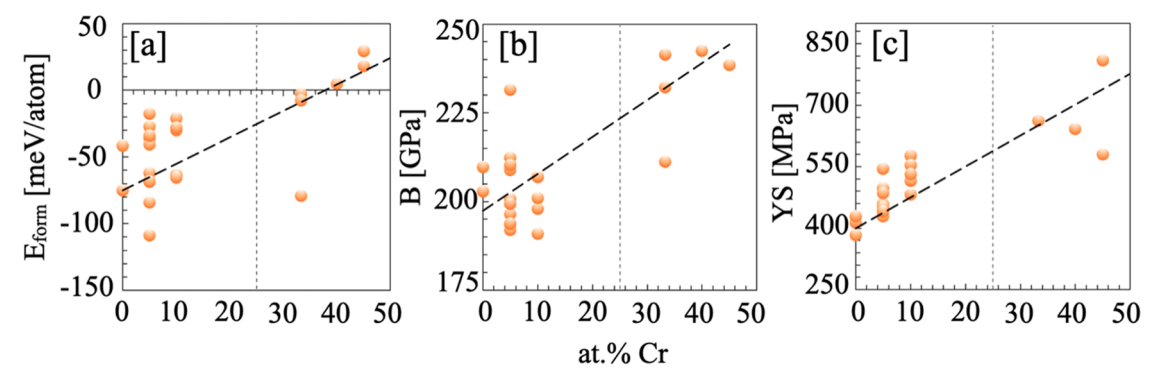


Fig. 9. (a) Formation energy (E_{form}), (b) bulk moduli (B), and (c) tensile strength (YS) of 20 down-selected RHEAs. The Cr-rich alloys were found to have higher thermal conductivity. See appendix for TC comparison with respect to valence electron count (Fig. A2(a)), Cr (Fig. A2(b)), and Cr+Mo+W (Fig. A3).

RHEAs are reported in Table 2.

It is evident from Table 2 that both DFT and CALPHAD provide reasonable estimates for the RT thermal conductivity of these five RHEAs. In general, DFT tends to overestimate the thermal conductivity of the alloys while CALPHAD show closer agreement with experiments. This is likely due to the fact that DFT assumes a perfect defect-free crystal lattice, causing thermal conductivity to be overestimated, on the other hand, CALPAHD uses thermal conductivity assessment from experiments. Indeed, CALPHAD thermal conductivity predictions for $Cr_{10}Mo_{25}Nb_{50}V_{15}$, $Cr_{10}Mo_{30}Nb_{30}Ti_5V_{25}$, and $Cr_{33}Mo_{33}Nb_{33}$ fall well within the standard deviations of the thermal conductivity measurements. For readers point of view, we want to clarify that the thermal conductivity measurements were conducted three times at various locations on the sample to confirm repeatability. Interestingly, out of three alloys one is ternary CrMoNb that shows excellent agreement. On the other hand, for remaining two alloys, CALPHAD over-predicts the thermal conductivity of Mo₂₅Nb₁₅Ti₁₀V₂₅W₂₅ and under-predicts for $Mo_{25}Nb_{50}V_{20}W_5$.

To put thermal conductivity measurement on five new RHEAs in context, we tabulated comparative literature data related to thermal conductivity measurements for several refractory alloys in Table 3. Notably, newly designed RHEAs show superior thermal conductivity compared to those reported in the literature [33,78], which area experimentally validated in Table 2. We also want to emphasize that our alloy design approach adopted in this work uses multiple RHEA down-selection constraints as detailed in Table 1 [43] while other alloys in literature only thermal conductivity related constraint [33,78]. To conclude, the higher thermal conductivity suggests that newly designed RHEAs may be better suited for thermal management in gas engine turbine blades.

3.7. Section VII - phonon connection to varying thermal conductivity in RHEAs

To connect thermal conductivity with elemental chemistry and element type on thermal conductivity, we analyzed phonon dispersion, density of states of CrMoNb, $Nb_{50}Mo_{25}V_{25}$, and $Nb_{50}Mo_{25}V_{20}W_5$ along

with their correlation with the average atomic mass.

The schematic in Fig. 10a illustrates the impact of random substitution in $Nb_{50}Mo_{25}V_{25}$ on mass disorder and electron-phonon coupling through overlapping phonon bands (Fig. 10b) in Nb-Mo-V with an atom of different mass and valence electrons. Fig. 10a suggests a higher phonon-dynamics, thereby, increasing thermal conductivity [79]. Notably, the tungsten substitution in $Nb_{50}Mo_{25}V_{25}$ (Fig. 10c) introduces higher mass disorder arising from its large atomic size and distinct valence electrons than (Nb,V), which is expected to reduce the overlap between phonon bands (Fig. 10d). The increased mass disorder reflects slower phonon transport and a consequent reduction in thermal conductivity. Furthermore, this could also be attributed to tailored electron-phonon coupling due to substituting the atoms with mixed valence electron count and high mass disorder such as tungsten.

Interestingly, based on the above hypothesis, we calculated and analyzed phononic and mass behavior for three selected RHEAs as shown in Fig. 11a-f. We found lower thermal conductivity in $Nb_{50}Mo_{25}V_{20}W_{5}$ compared CrMoNb $Nb_{50}Mo_{25}V_{25}$ to and {CALPHAD=43.12, DFT=47.8; Expt.= 42.09 ± 2.11) W/m-K; (CALPHAD=25.4 DFT=36.2) W/m-K; and (CALPHAD=27.97, DFT=33.5, Expt.=33.46 \pm 4.08) W/m-K}, which is attributed to disorder effects induced by tungsten addition. The introduction of tungsten by partially substituting vanadium atoms induce considerable mass disparity. Notably, tungsten is four times as massive as vanadium and twice as heavy as molybednum and niobium, which possibly leads to heightened mass-disorder scattering. In contrast, the presence of tungsten atoms on vanadium sites introduces an additional valence electron, thereby intensifying electron-phonon scattering—a phenomenon commonly associated with the aliovalent doping of atoms [80].

This increased disparity in atomic masses created by tungsten atoms contributes to a lower thermal conductivity than the $Nb_{50}Mo_{25}V_{25}$. Thus, incorporating tungsten into the alloy augments band crossings in the phonon band structure [81]. The reduced overlap between acoustic and optical modes arises from the substantial mass disparity between W atoms and the remaining constituents of the alloy matrix. This discrepancy induces a sluggishness in the acoustic modes. Further, the observed decrease in frequencies for both optical and acoustic phonons

 Table 2

 Nominal and EDS compositions, experimental measurements and predictions via CALPHAD for density, and experimental measurements and predictions via DFT and CALPHAD for thermal conductivity of the selected RHEAs.

Selected RHEAs Compo	sitions	Condition	Density [g/c	.c.]	Therma	al Conductivity [W/(m-K)]
Nominal	EDS		CALPHAD	Expt.	DFT	CALPHAD	Expt.
Cr ₁₀ Mo ₂₅ Nb ₅₀ V ₁₅	Cr _{9.8} Mo _{24.3} Nb _{50.1} V _{15.8}	VAM + 1800°C 10h	8.55	8.554	37.1	29.65	31.45 ± 2.20
$Cr_{10}Mo_{30}Nb_{30}Ti_5V_{25}$	$Cr_{9.2}Mo_{27.4}Nb_{32.1}Ti_{5.5}V_{25.8}$	$VAM + 1800^{\circ}C$ 12h	8.19	8.197	26.5	26.39	24.82 ± 1.61
Cr ₃₃ Mo ₃₃ Nb ₃₃	Cr _{33.8} Mo _{32.5} Nb _{33.7}	$VAM + 1800^{\circ}C 10h$	8.82	8.758	47.8	43.12	42.09 ± 2.11
$Mo_{25}Nb_{15}Ti_{10}V_{25}W_{25}$	$Mo_{25.5}Nb_{14.8}Ti_{9.4}V_{24.1}W_{26.2}$	$VAM + 1800^{\circ}C \ 20h + 1925^{\circ}C \ 14h$	10.75	10.645	35.7	32.01	25.53 ± 2.54
$Mo_{25}Nb_{50}V_{20}W_5$	$Mo_{24.5}Nb_{48.9}V_{21.4}W_{5.2}$	$VAM + 1925^{\circ}C$ 12h	9.07	8.959	33.1	27.97	33.46 ± 4.08

Table 3
Thermal conductivity comparison between this work (five RHEAs) and literature [33,78]. (VAM: Vacuum arc-melting. SPS: Spark plasma sintering).

Nominal compositions of selected RHEAs	EDS compositions of selected RHEAs	Conditions	Measured Thermal Conductivity [W/(m-K)]
Cr ₁₀ Mo ₂₅ Nb ₅₀ V ₁₅	Cr _{9.8} Mo _{24.3} Nb _{50.1} V _{15.8}	VAM + Homogenized (1800°C 10h)	31.45 ± 2.20
$Cr_{10}Mo_{30}Nb_{30}Ti_5V_{25}$	$Cr_{9.2}Mo_{27.4}Nb_{32.1}Ti_{5.5}V_{25.8}$	VAM + Homogenized (1800°C 12h)	24.82 ± 1.61
$Cr_{33}Mo_{33}Nb_{33}$	Cr _{33.8} Mo _{32.5} Nb _{33.7}	VAM + Homogenized (1800°C 10h)	42.09 ± 2.11
$Mo_{25}Nb_{15}Ti_{10}V_{25}W_{25}$	$Mo_{25.5}Nb_{14.8}Ti_{9.4}V_{24.1}W_{26.2}$	$VAM + Homogenized (1800^{\circ}C 20h + 1925^{\circ}C 14h)$	25.53 ± 2.54
$Mo_{25}Nb_{50}V_{20}W_5$	$Mo_{24.5}Nb_{48.9}V_{21.4}W_{5.2}$	VAM + Homogenized (1925°C 12h)	33.46 ± 4.08
TaTiNb [33]	NA	SPS (1373 K, 50 MPa, 10 min)	23
TaTiNbZr [33]	NA	SPS (1373 K, 50 MPa, 10 min)	14
TaTiNbZrMo [33]	NA	SPS (1373 K, 50 MPa, 10 min)	15
TaTiNbZrW [33]	NA	SPS (1373 K, 50 MPa, 10 min)	11
$W_{60}Ta_{20}V_{20}$ [78]	$W_{64.5}Ta_{21.3}V_{14.3}$	VAM	42
WTaV [78]	$W_{42.1}Ta_{33.5}V_{24.4}$	VAM	25
$W_{40}Ta_{20}V_{20}Ti_{20}$ [78]	$W_{37.5}Ta_{28.9}V_{17.8}Ti_{15.8}$	VAM	19
WTaVTiCr [78]	$W_{41.3}Ta_{25.7}V_{12.7}Ti_{9.7}Cr_{10.7} \\$	VAM	14

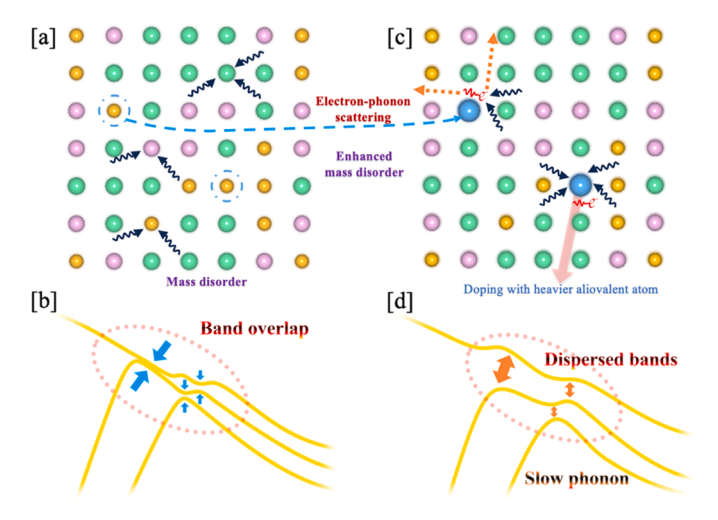


Fig. 10. Schematic showing the impact of aliovalent (an atom with distinct valence electrons) on (a) inherent mass-disorder, (b) bands indicative of fast phonon dynamics, (c) substitution by an atom of distinct valence electrons leads to (d) reduced band overlap in disordered solids.

indicate the presence of a phonon softening effect, leading to a reduction in group velocities and suppression of thermal transport.

Predominantly, tungsten influences mid-frequency bands, including acoustic bands' highest frequencies, as indicated by the states' phonon density. This complex interplay of mass variations and band structure alterations underscores the intricate relationship between alloy composition and lattice thermal conductivity in the Nb₅₀Mo₂₅V₂₀W₅. As tungsten content increases, the mean atomic mass of the system rises (Fig. 11f), causing W to transition from an impurity to a more integral part of the alloy matrix, thereby suppressing mass disorder and enhancing thermal transport. This leads to increased thermal conductivity for W-rich alloys. To corroborate these results, the thermal conductivities of three RHEAs were estimated with CALPHAD. The thermal conductivity of CrMoNb, $Nb_{50}Mo_{25}V_{25}$, and $Nb_{50}Mo_{25}V_{20}W_5$ were 43.12 (DFT=47.8; Expt.= 42.09 \pm 2.11) W/m-K, 25.4 (DFT=36.2) W/ m-K, and 27.97 (DFT=33.5; Expt.=33.46 \pm 4.08) W/m-K, respectively. The CALPHAD successfully predicted the highest thermal conductivity for CrMoNb, similar to DFT (47.82 W/m-K) and experiments (42.09 \pm 2.11 W/m-K). However, the CALPHAD-based calculations could not capture the effect of small composition variation on thermal conductivity of $Nb_{50}Mo_{25}V_{25}$ and $Nb_{50}Mo_{25}V_{20}W_5$. This also highlights the limitations of CALPHAD and stresses the importance of the systematic ab initio results in this work. Finally, in Fig. 11h, we show DFT calculated vibrational (lattice) entropy for the three alloys, which shows that alloy with maximum mass disorder, i.e., Nb₅₀Mo₂₅V₂₀W₅, has higher entropic contribution, which increases at elevated temperatures. Moreover, it is

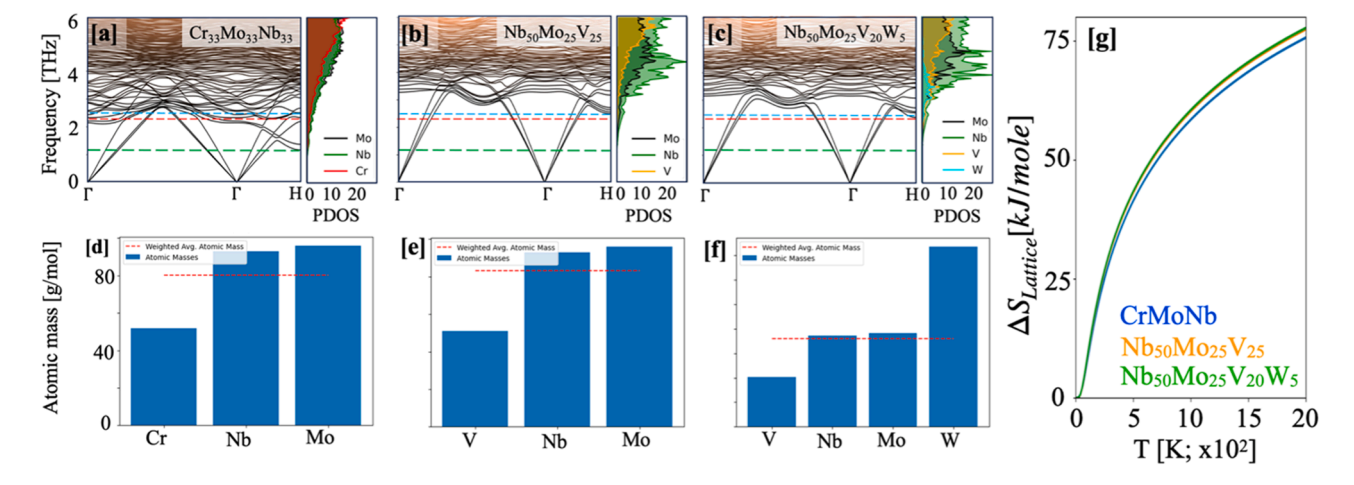


Fig. 11. Phonon dispersion and density of states displayed for (a) CrMoNb, (b) $Nb_{50}Mo_{25}V_{25}$, and (c) $Nb_{50}Mo_{25}V_{20}W_5$ RHEAs. (e-f) The mean atomic mass of respective elements in three RHEAs was analyzed to highlight their mass differences. The color of the dashed lines in (a-c) shows soft (green) to stronger (red) modes with change in disorder, while the red dashed line in (d-f) shows mean-atomic mass for respective RHEAs. (g) The lattice entropy vs temperature plot for three alloys showing higher mass disorder leads to higher entropic contribution.

well understood that phonon (optical) concentration increases with increasing temperature, which will lead to shorter relaxation times ($\sim 1/\mathrm{T})$ arising from increased phonon-phonon scattering, thereby, resulting into an inverse relationship between thermal conductivity and temperature [82]. This suggests that tungsten-based alloys will expected have much lower thermal conductivity at higher temperature, which is also reflected through increased density of optical phonons at higher frequencies. Notably, the lattice contribution was found to decrease systematically with decreasing mass disorder, which is minimum for CrMoNb.

The elevated thermal conductivity observed for CrMoNb is attributed to a symmetrical band structure, low mass disorder (Fig. 11d), and lower frequencies of acoustic vibrational modes, as shown in Fig 11a-c. In highly disordered alloys, phonons experience scattering proportional to the fourth power of phonon frequency (ω^4) [83,84], accentuating the significance of low-frequency acoustic modes in enhancing thermal conductivity by reducing the magnitude of scattering. Another contributing factor is the closely aligned behavior of Nb and Mo, which is evident in the density of states. This similarity in behavior reduces phonon scattering, further promoting efficient thermal transport in the alloy. The heightened intensity of the phonon DOS in the CrMoNb alloy indicates a substantial number of available pathways for phonon transport, thereby suggesting a higher thermal conductivity. Additionally, the increased density of phonons at lower frequencies underscores the alloy's superior capacity for thermal transport.

4. Conclusion

To achieve thermal stability and to reduce residual or operational thermal stresses inside components during their fabrication and thermomechanical processing, we must design alloys with enhanced thermal conductivity (or tailored thermal conductivity for other applications), which induces rapid heat dissipation from high-temperature regions. As such, we performed a systematic study using the DFT-based transport calculations for selected unary, binary, ternary, quaternary, and quinary refractory alloys and RHEAs, including relaxation times, along with electrical, thermal conductivity, and the Seebeck coefficient, to understand alloying effects on transport properties of Ti-Cr-Mo-W-V-Nb-Ta RHEAs. For simplicity, scattering from any kind of point defects was not considered. However, we were able to capture the contribution of individual alloying elements to thermal transport.

Our results provided an initial understanding of alloying effects introduced by chemical complexity and its impacts on the thermal transport of RHEAs. They show that increased entropy arising from increased chemical complexity in RHEAs gives control over the tunability of thermal transport. These insights into RHEA thermal behavior and their chemical and thermodynamic correlation provide an avenue for high-throughput exploration of charge-carrier tunability and direct design of new alloys with tailored thermal-transport performance using optimal alloying. Our CALPHAD and experimental results validated the findings of this work. Thermodynamic, electronic-structure, phonon, and mechanical property analysis show critical structure-

property correlations to enhance and tailor thermal transport in metal alloys. Our work provides a path forward in alloy design for hightemperature applications.

CRediT authorship contribution statement

Prashant Singh: Conceptualization, Data curation, Formal analysis, Funding acquisition, Investigation, Methodology, Project administration. Resources, Software, Supervision, Validation, Visualization, Writing – original draft, Writing – review & editing. Cafer Acemi: Data curation, Formal analysis, Investigation, Methodology, Writing - original draft. Aditya Kuchibhotla: Data curation, Formal analysis, Investigation, Writing - original draft. Brent Vela: Data curation, Formal analysis, Investigation, Methodology, Validation, Visualization, Writing - original draft. Prince Sharma: Data curation, Formal analysis, Investigation, Methodology, Validation, Visualization, Writing - original draft. Weiwei Zhang: Data curation, Software, Validation, Writing - review & editing. **Paul Mason:** Software, Writing - review & editing. Ganesh Balasubramanian: Resources, Supervision, Writing - review & editing. Ibrahim Karaman: Funding acquisition, Resources, Supervision, Writing - review & editing. Raymundo Arroyave: Conceptualization, Funding acquisition, Resources, Supervision, Writing - review & editing. M. Cynthia Hipwell: Funding acquisition, Resources, Supervision, Writing - review & editing. Duane D. Johnson: Funding acquisition, Resources, Supervision, Writing - review & editing.

Declaration of competing interest

The authors declare that they have no known competing financial interests or personal relationships that could have appeared to influence the work reported in this paper.

Acknowledgements

Authors acknowledge the U.S. Department of Energy (DOE) ARPA-E ULTIMATE Program through Project DE-AR0001427. BV acknowledges the support of NSF through Grant no. DGE-1545403 and acknowledges support from NSF through Grant no. 1746932. RA also acknowledges NSF through Grant No. 2119103. IK and CA acknowledge support from the NASA ESI Program through Grant No. 80NSSC21K0223. PSh and GB acknowledge support from NSF through Grant No. 1944040. PS acknowledges funding support (in part) from the Laboratory Directed Research and Development (LDRD) program at Ames National Laboratories related to understanding electronic and phononic structure of refractory metals. The work at Ames Laboratory was supported by the U. S. Department of Energy (DOE) Office of Science, Basic Energy Sciences, Materials Science & Engineering Division. Part of the research was performed at Iowa State University and Ames Laboratory, which is operated by ISU for the U.S. DOE under contract DE-AC02-07CH11358. High-throughput DFT calculations were carried out in part at the Texas A&M High- Performance Research Computing (HPRC) Facility.

Appendix

The electronic-structure and charge density of unary {Cr, Mo, W} and binary {CrMo, CrW, MoW} alloys. In charge density plot, we could clearly see the increasing complexity with increasing number of elements.

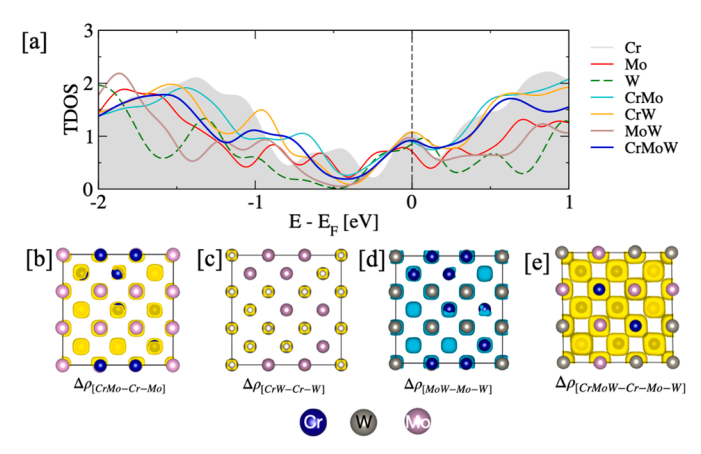


Fig. A1. (a) Electronic density of states, and (b-d) change in electronic charge density ($\Delta \rho$) for binary {CrMo, CrW, MoW}, and ternary CrMoW. The isosurface value of 0.12 e-/Å³ was used.

Thermal conductivity vs VEC and Cr concentration: In Fig. A2, we show correlation of DFT and CALPHAD calculated thermal (total) conductivity with valence electron count and chromium concentration Ti-Cr-Mo-W-V-Nb-Ta RHEAs. Appendix Fig. A2 (a) clearly shows an increasing trend in TC with increasing electron count, while TC plot with respect to pure Cr in Fig. A2 (b) does not so such trend.

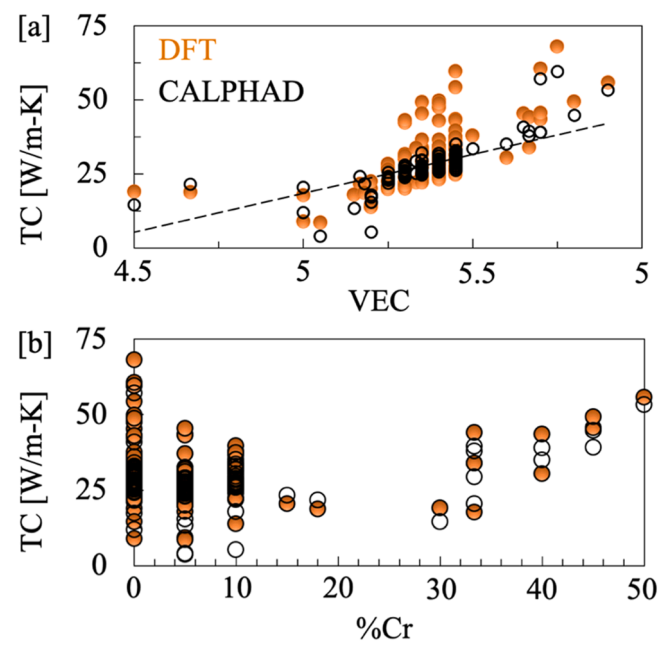


Fig. A2. Thermal (total) conductivity with respect to (a) valence electron count, and (b) chromium concentration in Ti-Cr-Mo-W-V-Nb-Ta RHEAs.

In Fig. A3, we show DFT calculated thermal (total) conductivity comparison with respect to the concentration of group VI elements, i.e., Cr+Mo+W, which shows good correlation. Figs. A2 (a) and A3 shows a more generalizable trend of TC in terms of VEC electron count rather than just one element type.

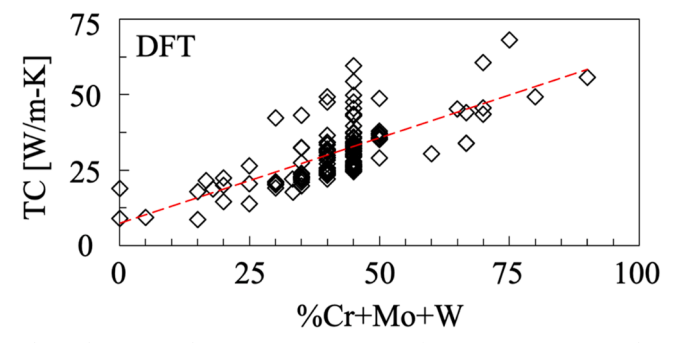


Fig. A3. DFT calculated thermal (total) conductivity with respect to composition of group VI (Cr+Mo+W) elements in Ti-Cr-Mo-W-V-Nb-Ta RHEAs.

References

- [1] J.W. Yeh, S.K. Chen, S.J. Lin, J.Y. Gan, T.S. Chin, T.T. Shun, C.H. Tsau, S.Y. Chang, Nanostructured high-entropy alloys with multiple principal elements: novel alloy design concepts and outcomes, Adv. Eng. Mater. 6 (2004) 299–303.
- [2] B. Cantor, I.T.H. Chang, P. Knight, A.J.B. Vincent, Microstructural development in equiatomic multicomponent alloys, Mater. Sci. Eng. A 375 (2004) 213–218.
- [3] D.B. Miracle, O.N. Senkov, A critical review of high entropy alloys and related concepts, Acta Mater. 122 (2017) 448–511.
- [4] B. Gludovatz, A. Hohenwarter, D. Catoor, E.H. Chang, E.P. George, R.O. Ritchie, A fracture-resistant high-entropy alloy for cryogenic applications, Science 345 (2014) 11531158 (1979).
- [5] P. Singh, A. Sharma, A.V. Smirnov, M.S. Diallo, P.K. Ray, G. Balasubramanian, D. D. Johnson, Design of high-strength refractory complex solid-solution alloys, npj Comput. Mater. 4 (1) (2018) 1–8.
- [6] Y. Lu, Y. Dong, S. Guo, L. Jiang, H. Kang, T. Wang, B. Wen, Z. Wang, J. Jie, Z. Cao, J. Ruan, T. Li, A promising new class of high-temperature alloys: eutectic highentropy alloys, Sci. Rep. 4 (2014) 1–5.
- [7] O.N. Senkov, D.B. Miracle, K.J. Chaput, J.P. Couzinie, Development and exploration of refractory high entropy alloys – a review, J. Mater. Res. 33 (2018) 3092–3128.
- [8] E.W. Huang, P.K. Liaw, High-temperature materials for structural applications: new perspectives on high-entropy alloys, bulk metallic glasses, and nanomaterials, MRS Bull. 44 (2019) 847–853.
- [9] O. El-Atwani, N. Li, M. Li, A. Devaraj, J.K.S. Baldwin, M.M. Schneider, J.S. Wróbel, D. Nguyen-Manh, S.A. Maloy, E. Martinez, Outstanding radiation resistance of tungsten-based high-entropy alloys, Sci. Adv. 5 (2019) eaav2002.
- [10] Y. Shi, B. Yang, P.K. Liaw, Corrosion-resistant high-entropy alloys: a review, Metals 7 (2017) 43 (Basel).
- [11] Y.K. Cao, et al., Precipitation behavior and mechanical properties of a hot-worked TiNbTa0.5ZrAl0.5 refractory high entropy alloy, Int. J. Refract. Met. Hard Mater. 86 (2020) 105132.
- [12] D. Ikeuchi, et al., Cr-Mo-V-W: a new refractory and transition metal high-entropy alloy system, Scr. Mater. 158 (2019) 141–145.
- [13] N.N. Guo, et al., Microstructure and mechanical properties of refractory MoNbHfZrTi high-entropy alloy, Mater. Des. 81 (2015) 87–94.
- [14] C.M. Lin, et al., Effect of Al addition on mechanical properties and microstructure of refractory AlxHfNbTaTiZr alloys, J. Alloys Compd. 624 (2015) 100–107.
- [15] F. Maresca, W.A. Curtin, Mechanistic origin of high strength in refractory BCC high entropy alloys up to 1900K, Acta Mater. 182 (2020) 235–249.
- [16] M. Moorehead, et al., High-throughput synthesis of Mo-Nb-Ta-W high-entropy alloys via additive manufacturing, Mater. Des. 187 (2020) 108358.
- [17] O.N. Senkov, et al., Microstructure and elevated temperature properties of a refractory TaNbHfZrTi alloy, J. Mater. Sci. 47 (9) (2012) 4062–4074.
- [18] O.N. Senkov, S.L. Semiatin, Microstructure and properties of a refractory highentropy alloy after cold working, J. Alloys Compd. 649 (2015) 1110–1123.
- [19] O.N. Senkov, et al., Mechanical properties of low-density, refractory multiprincipal element alloys of the Cr-Nb-Ti-V-Zr system, Mater. Sci. Eng. Struct.
- Mater. Prop. Microstruct. Process. 565 (2013) 51–62.
 [20] O.N. Senkov, C. Woodward, D.B. Miracle, Microstructure and properties of aluminum-containing refractory high-entropy alloys, JOM 66 (10) (2014) 2030–2042.
- [21] O.N. Senkov, C.F. Woodward, Microstructure and properties of a refractory NbCrMo0.5Ta0.5TiZr alloy, Mater. Sci. Eng. Struct. Mater. Prop. Microstruct. Process. 529 (2011) 311–320.
- [22] O.N. Senkov, et al., Oxidation behavior of a refractory NbCrMo0.5Ta0.5TiZr alloy, J. Mater. Sci. 47 (18) (2012) 6522–6534.
- [23] S. Sheikh, et al., Aluminizing for enhanced oxidation resistance of ductile refractory high-entropy alloys, Intermetallics 103 (2018) 40–51 (Barking).
- [24] N. Yurchenko, et al., Oxidation behavior of refractory AlNbTiVZr0.25 high-entropy alloy, Materials 11 (12) (2018) 2526.
- [25] P. Zhang, et al., Oxidation response of a vacuum arc melted NbZrTiCrAl refractory high entropy alloy at 800-1200 degrees C, Vacuum 162 (2019) 20–27.
- [26] H. Dobbelstein, et al., Laser metal deposition of a refractory TiZrNbHfTa high-entropy alloy, Addit. Manuf. 24 (2018) 386–390.
- [27] H. Dobbelstein, et al., Laser metal deposition of compositionally graded TiZrNbTa refractory high-entropy alloys using elemental powder blends, Addit. Manuf. 25 (2019) 252–262.
- [28] H. Dobbelstein, et al., Direct metal deposition of refractory high entropy alloy MoNbTaW, in: Proceedings of the Laser Assisted Net Shape Engineering 9 International Conference on Photonic Technologies Proceedings of the Lane 2016, Amsterdam, Elsevier Science Bv, 2016, pp. 624–633. M. Schmidt, F. Vollertsen, and C.B. Arnold, Editors.
- [29] I.M. Kunce, Polanski, J. Bystrzycki, Microstructure and hydrogen storage properties of a TiZrNbMoV high entropy alloy synthesized using Laser Engineered Net Shaping (LENS), Int. J. Hydrog. Energy 39 (18) (2014) 9904–9910.
- [30] X.Y. Ding, H.Y. Zheng, P.P. Zhnag, L.M. Luo, Y.C. Wu, J.H. Yao, Microstructure and mechanical properties of WTaVCrTi refractory high-entropy alloy by vacuum levitation melting for fusion applications, J. Mater. Eng. Perform. 32 (2022) 7869–7878.
- [31] Y. Li, Y. Sun, L. Chneg, Y. Yuan, B. Jia, J. He, G.N. Lu, Q. Zhu, Preliminary exploration of a WTaVTiCr h[igh-entropy alloy as a plasma-facing material, Nucl. Fusion 62 (2022) 126002.
- [32] Y. Dong, S. Mu, X. Guo, J. Han, J. Duan, N. Jia, Y. Xue, K. Jin, Transport properties of refractory high-entropy alloys with single-phase body-centered cubic structure, Scr. Mater. 231 (2023) 115464.

- [33] N.F. Shkodich, K.V. Kuskov, A.S. Sedegov, I.D. Kovalev, A.V. Panteleeva, Y. S. Vergunova, Y.B. Scheck, E. Panina, N. Stepanov, I. Serhiienko, D. Moskovskikh, Refractory TaTiNb, TaTiNbZr, and TaTiNbZrX (X = Mo, W) high entropy alloys by combined use of high energy ball milling and spark plasma sintering: Structural characterization, mechanical properties, electrical resistivity, and thermal conductivity, J. Alloys. Compd. 893 (2022) 162030.
- [34] H.I. Jeong, C.M. Lee, D.H. Kim, Manufacturing of Ti–Nb–Cr–V–Ni high entropy alloy using directed energy deposition and evaluation of materials properties, J. Mater. Res. Technol. 23 (2023) 5606–5617.
- [35] J.L. Bartlett, X. Li, An overview of residual stresses in metal powder bed fusion, Addit. Manuf. 27 (2019) 131–149.
- [36] S. Shafeie, S. Guo, Q. Hu, H. Fahlquist, P. Erhart, A. Palmqvist, High-entropy alloys as high-temperature thermoelectric materials, J. Appl. Phys. 118 (2015) 184905.
- [37] Z. Fan, H. Wang, Y. Wu, X.J. Liu, Z.P. Lu, Thermoelectric high-entropy alloys with low lattice thermal conductivity, RSC Adv. 6 (2016) 52164–52170.
- [38] Z. Fan, H. Wang, Y. Wu, X. Liu, Z. Lu, Thermoelectric performance of PbSnTeSe high-entropy alloys, Mater. Res. Lett. 5 (2017) 187–194.
- [39] M.J. Abere, E. Ziade, P. Lu, C.B. Saltonstall, X. Gu, W.J. Wright, N. Argibay, A. B. Kustasa, A predictive analytical model of thermal conductivity for aluminum/transition metal high-entropy alloys, Scr. Mater. 208 (2022) 114330.
- [40] B. Vela, C. Acemi, P. Singh, et al., High-throughput exploration of the WMoVTaNbAl refractory multi-principal-element alloys under multiple-property constraints, Acta Mater. 248 (2023) 118784.
- [41] D. Khatamsaz, B. Vela, P. Singh, D.D. Johnson, D. Allaire, R. Arróyave, Bayesian optimization with active learning of design constraints using an entropy-based approach, npj Comput. Mater. 9 (1) (2023) 49.
- [42] G. Vazquez, P. Singh, D. Sauceda, R. Couperthwaite, N. Britt, et al., Efficient machine-learning model for fast assessment of elastic properties of high-entropy alloys, Acta Mater. 232 (2022) 117924.
- [43] Advanced Research Projects Agency-Energy, Ultrahigh temperature impervious materials advancing turbine efficiency (ULTIMATE). 2020.
- [44] X. Zheng, D. Cahill, P. Krasnochtchekov, R. Averback, J. Zhao, High-throughput thermal conductivity measurements of nickel solid solutions and the applicability of the Wiedemann–Franz law, Acta Mater. 55 (2007) 5177–5185.
- [45] X. Chong, M. Hu, P. Wu, Q. Shan, Y. Jiang, Z. Li, J. Feng, Tailoring the anisotropic mechanical properties of hexagonal M7X3 (M = Fe, Cr,W, Mo; X = C, B) by multialloying, Acta Mater. 169 (2019) 193–208.
- [46] K. Li, E. Kim, Y. Fehlis, D. Persaud, B. DeCost, M. Greenwood, J. Hattrick-Simpers, A call for caution in the era of AI-accelerated materials science, Matter 6 (12) (2023) 4116–4117.
- [47] J. Schrier, A.J. Norquist, T. Buonassisi, J. Brgoch, Pursuit of the exceptional: research directions for machine learning in chemical and materials science, J. Am. Chem. Soc. 145 (40) (2023) 21699–21716
- [48] P. Singh, et al., Theory-guided design of duplex-phase multi-principal-element alloys Author links open overlay, Acta Mater. 272 (2024) 119952.
- [49] G. Kresse, J. Hafner, Ab initio molecular dynamics for liquid metals, Phys. Rev. B 47 (1993) 558–561.
- [50] G. Kresse, D. Joubert, From ultrasoft pseudopotentials to the projector augmentedwave method, Phys. Rev. B 59 (1999) 1758–1775.
- [51] J.P. Perdew, K. Burke, M. Ernzerhof, Generalized gradient approximation made simple, Phys. Rev. Lett. 77 (1996) 3865–3868.
- [52] P. Singh, M.K. Harbola, B. Sanyal, A. Mookerjee, Accurate determination of band gaps within density functional formalism, Phys. Rev. B 87 (2013) 235110.
- [53] P. Singh, M.K. Harbola, M. Hemanadhan, A. Mookerjee, D.D. Johnson, Better band gaps with asymptotically corrected local exchange potentials, Phys. Rev. B 93 (2016) 085204.
- [54] A. P. Söderlind, P. Turchi, P.E.A. Landa, V. Lordi, Ground-state properties of rareearth metals: an evaluation of density-functional theory J. Phys. 26 (2014) 416001.
- [55] T.J. Giese, D.M. York, A GPU-accelerated parameter interpolation thermodynamic integration free energy method, J. Chem. Theory Comput. 14 (2018) 1564–1582.
- [56] H.J. Monkhorst, J.D. Pack, Special points for Brillouin-zone integrations, Phys. Rev. B 13 (1976) 5188–5192.
- [57] R. Singh, et al., Accelerating computational modeling and design of high-entropy alloys, Nat. Comput. Sci. 1 (2021) 54.
- [58] A. Togo, I. Tanaka, First principles phonon calculations in materials science, Scr. Mater. 108 (2015) 1–5.
- [59] G.K.H. Madison, D.J. Singh, BoltzTraP. A code for calculating band-structure dependent quantities, Comput. Phys. Commun. 175 (2006) 67.
- [60] G.A. Slack, Nonmetallic crystals with high thermal conductivity, J. Phys. Chem. Solids 34 (1973) 321.
- [61] G.A. Slack, The thermal conductivity of nonmetallic crystals, J. Phys. C Solid St. Phys. 34 (1979) 1.
- [62] G.C. Fletcher, M. Yahaya, The electronic Gruneisen parameter for the transition metals, J. Phys. F Met. Phys. 9 (1979) 1529.
- [63] Q. Chen, B. Sundman, Calculation of debye temperature for crystalline structures—a case study on Ti, Zr, and Hf Author links open overlay panel, Acta Mater. 49 (2001) 947–961.
- [64] M.A. Blanco, E. Francisco, V. Luana, GIBBS: isothermal-isobaric thermodynamics of solids from energy curves using a quasi-harmonic Debye model, Comput. Phys. Commun. 158 (1) (2004) 57–72.
- [65] M.A. Blanco, A.M. Pendas, E. Francisco, J.M. Recio, R. Franco, Thermodynamical properties of solids from microscopic theory: applications to MgF2 and Al2O3, J. Mol. Struct. Theochem. 368 (1996) 245–255.
- [66] J.P. Poirier, Introduction to the Physics of the Earth's Interior, 2nd ed., Cambridge University Press, 2000.

- [67] Thermo-Calc, Thermo-Calc Documentation, 2022. https://thermocalc.com/support/documentation.
- [68] D.T. Morelli, J.P. Heremans, G.A. Slack, Estimation of the isotope effect on the lattice thermal conductivity of group IV and group III-V semiconductors, Phys. Rev. B 66 (19) (2002) 195304.
- [69] M.N. Luckyanova, et al., Coherent phonon heat conduction in superlattices, Science 338 (6109) (2012) 936–939 (1979).
- [70] Q. Zheng, P.V. Braun, D.G. Cahill, Thermal conductivity of graphite thin films grown by low temperature chemical vapor deposition on Ni (111), Adv. Mater. Interfaces 3 (16) (2016) 1600234.
- [71] A. Schmidt, Thesis: Optical characterization of thermal transport from the nanoscale to the macroscale, 2009.
- [72] D.G. Cahill, Analysis of heat flow in layered structures for time-domain thermoreflectance, Rev. Sci. Instrum. 75 (2004) 5119–5122.
- [73] M. Mukherjee, S. Satsangi, A.K. Singh, A statistical approach for the rapid prediction of electron relaxation time using elemental representatives, Chem. Mater. 32 (2020) 6507–6514.
- [74] Electrical of the elements 2024 https://periodictable.com/Properties/A/ElectricalConductivity.v.wt.html.
- [75] Conductivity M. Upadhyaya, C.J. Boyle, D. Venkataraman, et al., Effects of disorder on thermoelectric properties of semiconducting polymers, Sci. Rep. 9 (2019) 5820.

- [76] P. Singh, et al., A ductility metric for refractory-based multi-principal element alloys, Acta Mater. 257 (2023) 1–15.
- [77] D.D. Johnson, P. Singh, A.V. Smirnov, N. Argibay, Universal maximum strength of solid metals and alloys, Phys. Rev. Lett. 130 (2023) 166101.
- [78] I.H. Kim, H.S. Oh, K.S. Lee, E.S. Park, Optimization of conflicting properties via engineering compositional complexity in refractory high entropy alloys, Scr. Mater. 199 (2021) 113839.
- [79] P Sharma, P Singh, G Balasubramanian, Engineering phonon transport through cation disorder in dimensionally constricted high entropy MXene, Carbon 223 (2024) 119015. N. Y.
- [80] S. Han, S. Dai, J. Ma, et al., Strong phonon softening and avoided crossing in aliovalence-doped heavy-band thermoelectrics, Nat. Phys. 19 (2023) 1649–1657.
- [81] M. Christensen, A. Abrahamsen, N. Christensen, et al., Avoided crossing of rattler modes in thermoelectric materials, Nat. Mater. 7 (2008) 811–815.
- [82] C.Y. Ho, R.W. Powell, P.E. Liley, Thermal conductivity of the elements, J. Phys. Chem. Ref. Data 1 (1972) 279–421.
- [83] C. Herring, Role of low-energy phonons in thermal conduction, Phys. Rev. 95 (1954) 954.
- [84] P.C.K. Kwok, Green's function method in lattice dynamics, Solid State Phys. 20 (1968) 213–303.